RELIABILITY OF TIME-LINEARIZED FLUTTER PREDICTIONS NEAR THE SURGE LINE

Markus May [*] *- Dr. Björn Grüber* [**]

[*] DLR – German Aerospace Center, Institute of Aeroelasticity
Bunsenstr. 10, 37073 Göttingen, Germany
Markus.May@dlr.de

[**] MTU Aero Engines GmbH, Compressor Aerodynamics/Aeroelasticity
Dachauer Str. 665, 80995 München, Germany
Bjoern.Grueber@mtu.de

ABSTRACT

In the context of the flutter analysis of a modern transonic axial compressor two different CFD codes have been compared: based on the same three-dimensional steady solution, the time-linearized Navier-Stokes flow solver TRACE of the German Aerospace Center DLR as well as the industrial time-linearized Euler code Lin3D (developed at MTU Aero Engines) were used to assess the global aerodynamic damping of the rotor.
No major differences could be observed for operating points on the working line. However, several operating points (at different shaft speeds) near the surge line were susceptible to flutter according to TRACE whereas Lin3D predicted aeroelastic stability.
The capturing of shock movements as well as the modeling of the tip gap is identified to be responsible for these discrepancies. In this paper the sources of the different local excitation and damping mechanisms are highlighted. Moreover influence coefficient representations for the different approaches are compared in the complex plane.

NOMENCLATURE

A_0	surface area of reference blade
$\boldsymbol{C_{\sigma_n}}$	unsteady aerodynamic coefficient matrix
$\hat{C}_p$	unsteady pressure coefficient
$\boldsymbol{E}$	transformation matrix
E_{kin}^{max}	maximum kinetic energy of the mode
$\vec{F}_c$, $\vec{F}_v$	convective and viscous flux vector
$\vec{G}_i$	generalized aerodynamic forces (GAF)
$\boldsymbol{I}$	identity matrix
$\boldsymbol{K}$	generalized stiffness matrix
$\boldsymbol{L}$	influence coefficient matrix
$\boldsymbol{M}$	generalized mass matrix
M_0	generalized mass of reference blade
N	number of blades, here $N = 19$
$\vec{R}$	residual vector
$\vec{S}$	source term vector
T	period of oscillation
$\vec{U}$	vector of conservative variables
V	cell volume
W_c	aerodynamic work per cycle
c	chord length
$\vec{f}_i$	aerodynamic forces
j	imaginary unit
$\vec{n}$	outward normal on the blade surface
p_{t1}, p_1	total and static pressure at inlet
$\vec{q}_i$, $\vec{q}_{\sigma_n}$	individual generalized coordinates
t	time
$\vec{x}$	position of mesh points
y^+	non-dimensional wall distance
Λ	aerodynamic damping (log. dec.)
$\boldsymbol{\Phi}$	structural modal basis
$\epsilon_{\xi\eta}$	local excitation in body-fitted coordinates
$\vec{\phi}$	(normalized) natural vibration mode
σ_n	inter-blade phase angle (IBPA), $\sigma_n = \frac{2\pi n}{N}$
ω	angular frequency of vibration, $\omega = 2\pi f$
$\Re(\ )$	real part of ( )
$\Im(\ )$	imaginary part of ( )

INTRODUCTION

Time-linearized flow solvers have proven to be efficient tools for predicting aeroelastic phenomena in turbomachines. One of the first implementations by Hall (1987) was based on solving the linearized Euler equations to analyze the unsteady flow in turbomachinery. Further developments (e.g. Holmes and Lorence (1998), Clark and Hall (2000), Sbardella and Imregun (2001) or Campobasso and Giles (2002)) extended this approach to two- and three-dimensional viscous flow regimes, by solving the linearized Navier-Stokes equations for flutter and forced response calculations. Mainly due to the reduction of computational costs these methods have become popular in the industrial context since they fulfill the requirement of short response times in the design process.

As the linearization about a steady state solution is performed, it is obvious that the phenomenon of interest – for example flow separation or a shock – already has to be present in the steady flow field in order to predict unsteady results accurately. Nevertheless it is questionable at which point the assumption of small harmonic perturbations does not hold true any more. This might especially be the case for operating points near the surge line of a compressor where strong shocks and flow separation dominate the steady solution.
Exactly this subject shall be addressed in the present paper by a detailed comparison of two operating points of a modern fan stage at part speed: one on the working line and the other one near the surge line.

THEORETICAL CONCEPTS

Aeroelastic Modeling

The governing aeroelastic equations of motion in generalized blade coordinates $\vec{q_i}$ yield

$$\boldsymbol{M}\ddot{\vec{q}}_i(t) + \boldsymbol{K}\vec{q}_i(t) = \boldsymbol{\Phi}^H \vec{f}_i(t) = \vec{G}_i(t), \tag{1}$$

where $\boldsymbol{M}$ and $\boldsymbol{K}$ are generalized mass and stiffness matrix respectively. For a detailed derivation please refer to the AGARD Manual on "Aeroelasticity in Axial-Flow Turbomachines" (Platzer and Carta, 1987/88). Structural damping has already been neglected in Equation (1). Since we are dealing with a modern blisk (integrally bladed rotor), hardly any mechanical damping is present and flutter susceptibilty can directly be deduced from the sign of the aerodynamic damping value.
It shall be mentioned that in this generalized modal form the equations of motion represent energy equations, where the generalized aerodynamic forces (GAF) on the right-hand side express the work done by the motion induced unsteady aerodynamic loads in the displacements of the individual mode shapes $\vec{\phi}_i^{(r)}$ for $r = 1, 2, ..., R$.
The vector of unsteady aerodynamic forces acting on the i-th blade depends on its own blade motion as well as on its neighbors'. The time history of these movements is taken into account by the inter-blade phase angle (IBPA)

$$\sigma_n = \frac{2\pi n}{N} \quad \text{with} \quad n = 0, 1, \ldots, N-1. \tag{2}$$

This fundamental concept formulated by Lane (1956) describes a traveling wave in which all N blades are oscillating harmonically with a certain (constant) phase shift of σ_n, whereas mode shape and vibration frequency are identical.
As outlined by Kemme (2004) the motion induced unsteady aerodynamic forces for the blades oscillating in the respective traveling wave modes can be expressed as

$$G_i(t) = (p_{t1} - p_1)A_0 \sum_{n=0}^{N-1} C_{\sigma_n} \hat{q}_{\sigma_n} e^{j(\omega t + i\sigma_n)}, \tag{3}$$

where $(p_{t1} - p_1)$ denotes the dynamic pressure at the entry and A_0 is the surface area of the blade. The non-dimensional complex coefficients C_{σ_n} can be deduced from the unsteady aerodynamic pressure distribution $\hat{C}_p$ on the blade oscillating with the inter-blade phase angle σ_n in the modal form $\vec{\phi}$.

Influence Coefficients

The kinematic relationship between all traveling wave motions and the displacement of all blades $i = 0, 1, \ldots, N-1$ writes

$$\vec{q}_i(t) = \boldsymbol{E}\vec{\hat{q}}_{\sigma_n} e^{j\omega t}, \tag{4}$$

where $\hat{q}_{\sigma_n}$ is the amplitude of the traveling wave mode with inter-blade phase angle σ_n. The matrix elements of $\boldsymbol{E}$ are defined as $E_{i,n} = e^{j\frac{2\pi in}{N}}$ for $i, n = 0, 1, \ldots, N-1$. Assuming a perfectly tuned system ($\boldsymbol{M} = M_0\boldsymbol{I}$, $\boldsymbol{K} = M_0\omega_0^2\boldsymbol{I}$ and $\vec{\phi}_i = \vec{\phi}_0$) and introducing Equations (3,4) in (1) finally leads to the flutter stability equations in two different forms: in traveling wave coordinates

$$-\omega^2 M_0 \boldsymbol{I}\vec{\hat{q}}_{\sigma_n} + M_0\omega_0^2\boldsymbol{I}\vec{\hat{q}}_{\sigma_n} = (p_{t1} - p_1)A_0\boldsymbol{C_{\sigma_n}}\vec{\hat{q}}_{\sigma_n} \tag{5}$$

as well as in blade coordinates

$$-\omega^2 M_0 \boldsymbol{I}\vec{\hat{q}}_i + M_0\omega_0^2\boldsymbol{I}\vec{\hat{q}}_i = (p_{t1} - p_1)A_0\boldsymbol{L}\vec{\hat{q}}_i. \tag{6}$$

The elements of the cyclic influence coefficient matrix

$$\boldsymbol{L} = \boldsymbol{E}\boldsymbol{C_{\sigma_n}}\boldsymbol{E}^{-1} = \begin{bmatrix} L_0 & L_{N-1} & L_{N-2} & \cdots & L_1 \\ L_1 & L_0 & L_{N-1} & & L_2 \\ L_2 & L_1 & L_0 & \ddots & \vdots \\ \vdots & & \ddots & \ddots & L_{N-1} \\ L_{N-1} & L_{N-2} & \cdots & L_1 & L_0 \end{bmatrix} \tag{7}$$

denote the aerodynamic influence of a specific blade on another one. Whereas the self-influence of the reference blade (index 0) is of constant stabilizing nature, the immediate neighbors (indices 1 and $N-1$) give a harmonically varying contribution, which can be seen as first harmonic oscillation in inter-blade phase angle. Accordingly, blades arranged further away contribute with the corresponding higher harmonic variation. Numerous studies – Hanamura et al. (1980) and Carta and St.Hilaire (1980) amongst others – revealed that the influence rapidly decreases with increasing distance from the reference blade and attains convergence after blade pair ± 2.
Applications of this theory with respect to experimental setups can be found in Hennings (1997) and Vogt (2005) who applied the transformation from influence coefficients to traveling wave modes in order to determine the aeroelastic stability behaviour of compressor and turbine cascades, respectively.

Energy Method

The classical approach for numerical flutter analysis of turbomachines is based on the energy method that was developed by Carta (1967) and has stood the test of time.
It assumes that the effects of aerodynamic forces on the structural dynamics properties of the aeroelastic system can be neglected, i.e. there will be no changes of mode shapes and eigenfrequencies due to unsteady aerodynamic blade loadings. Accordingly, one deals with a weakly coupled problem and can thus determine eigenmodes and natural frequencies in advance.
The prescribed motion of the blades – resulting from the respective eigenbehaviour of the rotor –,

leads to unsteady airloads by means of pressure variations $\hat{p}$ on the blade surface. The global aerodynamic work per cycle W_c describes the work exerted by the fluid on a given blade within one period of its motion. In this context a positive work entry ($W_c > 0$) indicates that energy is transfered from the air flow to the structure exciting the blade. For a negative work entry ($W_c < 0$) in contrast, the blade releases energy so that oscillations are damped. The respective damping value in terms of logarithmic decrement can be deduced as

$$\Lambda = -\frac{W_c}{2E_{kin}^{max}}, \tag{8}$$

where the maximum kinetic energy is given by $E_{kin}^{max} = \frac{1}{2}M_0\omega_0^2$ with modal mass M_0 and angular frequency ω_0 of the mode shape. Locally, the excitation of cell $\xi\eta$ with surface area $A_{\xi\eta}$ is represented by

$$\epsilon_{\xi\eta} = \frac{W_{c,\,\xi\eta}}{2E_{kin}^{max}\,A_{\xi\eta}}. \tag{9}$$

NUMERICAL APPROACH

Nonlinear Time-Accurate Methods

The TRACE code – developed at DLR for internal flows, especially in turbomachinery – has been applied to perform the steady Reynolds-averaged Navier-Stokes (RANS) computations in this article. It is in use at several German universities and represents the standard CFD tool for steady flow simulations at MTU Aero Engines in Munich.
The general system of conservation laws yields

$$\frac{\partial\vec{U}}{\partial t} + \frac{\partial\vec{F}_i(\vec{U})}{\partial x_i} + \vec{S}(\vec{U}) = \vec{0} \tag{10}$$

where $\vec{U}$ denotes the state vector of conservative variables, $\vec{F}_i(\vec{U}) = \vec{F}_{c_i}(\vec{U}) - \vec{F}_{v_i}(\vec{U})$ and $\vec{S}(\vec{U})$ the convective and viscous fluxes (with respect to coordinates x_i) and the source terms, respectively. To address aeroelastic problems with a moving mesh Equation (10) has to be rewritten in Arbitrary Lagrangian Eulerian (ALE) formulation before the spatial discretization in finite volumes is carried out:

$$\frac{\partial(V\vec{U})}{\partial t} + V\vec{R}(\vec{U},\vec{x},\dot{\vec{x}}) = \vec{0}, \tag{11}$$

where V shall indicate the cell volume that varies in time. The residual $\vec{R}$ depends on the flow variables $\vec{U}$ as well as on the grid coordinates $\vec{x}$ and velocities $\dot{\vec{x}}$ in order to account for the additional fluxes due to mesh deformation.

Time-Linearized Methods

At DLR, the first time-linearized solvers have been developed by Hagenah (2004) and Petrie-Repar (2006). This finally led to an integration in the environment of the TRACE code (Kersken et al., 2010).
Based on the assumption of small harmonic perturbations, the coordinates of the grid vertices $\vec{x}$ as well as the flow solution can be decomposed in a steady part (independant from time) and a time-dependant harmonic perturbation:

$$\vec{x}(t) = \vec{x}_0 + \Re\left(\hat{\vec{x}}(\vec{x}_0)e^{j\omega_0 t}\right) \tag{12}$$

$$\vec{U}(\vec{x}_0,t) = \vec{U}_0(\vec{x}_0) + \Re\left(\hat{\vec{U}}(\vec{x}_0)e^{j\omega_0 t}\right) \tag{13}$$

where ω_0 is again the angular frequency of the considered mode. Taking into account a linearized approximation of the nonlinear residual and introducing Equations (13) in (11) finally results in the following system of linear equations:

$$\left(j\omega_0 + \frac{\partial \vec{\boldsymbol{R}}}{\partial \vec{\boldsymbol{U}}} \right) \vec{\hat{U}} = - \left(\frac{\partial \vec{\boldsymbol{R}}}{\partial \vec{\boldsymbol{x}}} \vec{\hat{x}} + \frac{\partial \vec{\boldsymbol{R}}}{\partial \dot{\vec{\boldsymbol{x}}}} j\omega_0 \vec{\hat{x}} + j\omega_0 \frac{\hat{V}}{V_0} \vec{U}_0 \right). \tag{14}$$

It shall be mentioned that the turbulence model has not been linearized; the constant eddy viscosity assumption was used instead. However, it is understood that this might not be suitable for complex flow conditions with seperation.

The difference between this approach and the time-linearized Euler method Lin3D developed by Kahl (2002) is the neglect of viscous flux contributions $\frac{\partial \vec{\boldsymbol{F}}_v}{\partial \vec{\boldsymbol{U}}}$ in the implementation of the term $\frac{\partial \vec{\boldsymbol{R}}}{\partial \vec{\boldsymbol{U}}}$ on the one hand and, of course, the interpolation of the steady flow solution onto a coarser Euler mesh with straight H-topology. On the opposite side linear TRACE, implemented via finite differences of the nonlinear flux routines of the time-accurate solver, uses the initial Navier-Stokes grid. Nevertheless, the application of a linearized Euler method on a steady Navier-Stokes solution is justified by the assumption that the perturbations detected by a time-linearized Euler solver propagate on the characteristics of the steady Navier-Stokes flow field. Linearizing around a – compared to steady Euler – more accurate steady RANS solution the hyperbolic problem, that is to say the transonic shock motion, can be captured by a linear Euler method. This holds true as long as there is no significant unsteady interaction between the shock and the boundary layer, i.e. the boundary layer thickness is supposed to be constant in the close vicinity (small amplitudes!) of the shock and the implications due to viscous perturbations are assumed to be negligible.

With respect to mesh deformation elliptic algorithms are employed to handle the displacement of the grid vertices before starting the time-linearized flow simulation in the frequency domain. From a numerical point of view, TRACE solves the resulting linear system of equations using a parallelized generalized minimal residual (GMRES) method with a symmetric successive over-relaxation (SSOR) preconditioner. Lin3D, in contrast, uses a pseudo-time marching algorithm based on a 3-stage Runge-Kutta scheme with local time stepping. Giles' non-reflecting boundary conditions were stipulated in both cases for the unsteady computations.

AEROLIGHT COMPRESSOR STAGE

In the context of the national research project AeroLight an automated aerodynamic optimization of a transonic axial compressor has been performed, including new design concepts based on current material research and innovative methods of construction. Whereas the initial blade design was shaped with in-house S2- and S1-procedures at the DLR Institute of Propulsion Technology, the further design loops were driven by optimization strategies described in Siller et al. (2009) and Siller and Aulich (2010).

Vasanthakumar et al. (2010) from the DLR Institute of Aeroelasticity carried out a detailed flutter analysis for the whole operating range of the rotor (cf. Figure 6) consisting of $N = 19$ blades. Furthermore a sensitivity study comparing the stability behaviour of different design loops and a variation of aeroelastic similarity parameters was presented recently by one of the authors (May, 2010).

Steady Flow Solution

The steady flow field was determined using the implicit Reynolds-averaged Navier-Stokes solver of the DLR TRACE code with the two-equation Wilcox $k\omega$ model as basis for turbulence closure.

Fourier boundary conditions were used to prescribe radial inlet profiles for Mach number, total pressure and temperature as well as the static outlet pressure of the complete stage (radial equilibrium). The complete wall treatment – at hub, casing and on the blade – was done using logarithmic wall functions with mean values for the dimensionless wall distance $y^+ \approx 10$.

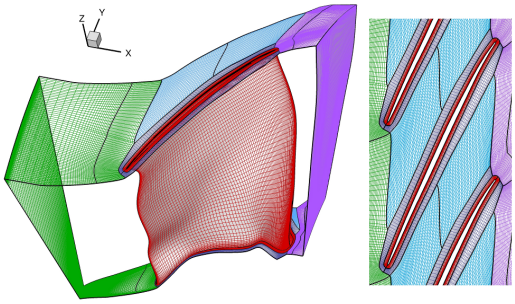

Figure 1: **CFD mesh of the rotor row**

The computational grid for the whole compressor stage consists of roughly 1.9 million hexahedras (single passage), half of whose are part of the rotor row illustrated on the left of Figure 1. The right-hand side shows the profile surrounded by an O-block followed by a C-block. Several H-blocks model inlet and passage sections as well as the exit of the row terminating with a mixing plane. A separate gap block at the tip of the blade completes the mesh.

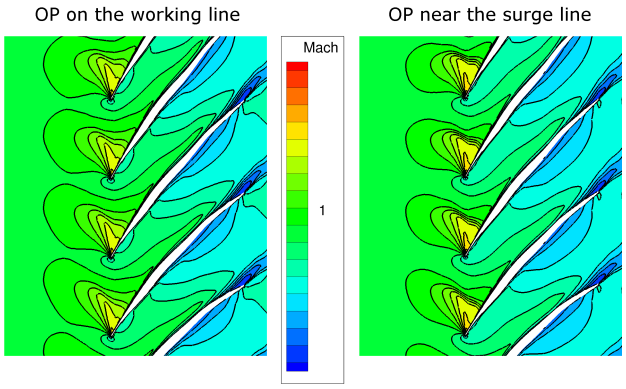

Figure 2: **Steady flow solution at midspan**

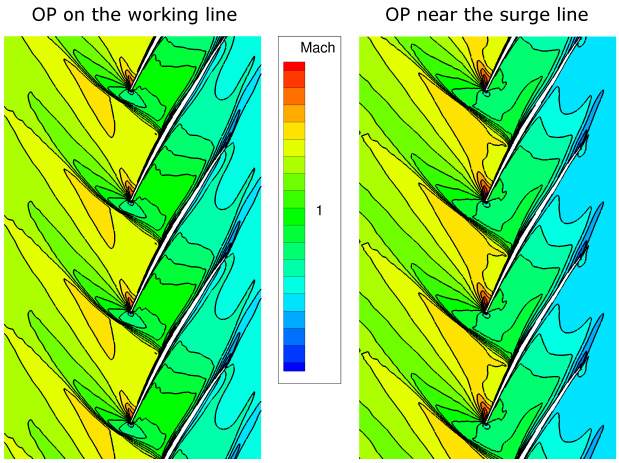

Figure 3: **Steady flow solution at** 90% **span**

Figures 2 and 3 illustrate contour plots of the Mach number distribution at 50% and 90% span, respectively. For a constant shaft speed an operating point (OP) on the working line (WL) is compared with another one near the surge line (SL): a stronger shock in lambda pattern can be stated for the throttled OP, especially for the outer part of the blade.

Global Unsteady Results

The eigenmodes of the rotor were determined by means of finite element analysis using the open-source software package CalculiX.

Figure 4 shows the first three mode shapes: two flexural modes and a chordwise bending. There is a strong increase in twist of the cross-sections in spanwise direction. Moreover an additional sharp bend diagonally across the blade is characteristic. That is why the blade itself is relatively stiff at hub and trailing edge, whereas the tip region of the leading edge will be the driving force in regard to aeroelastic stability or instability.

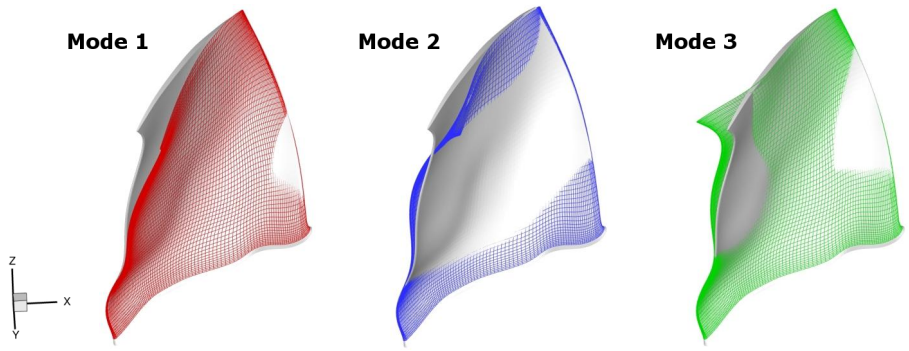

Figure 4: **Deformed CFD mesh according to the first three structural eigenmodes**

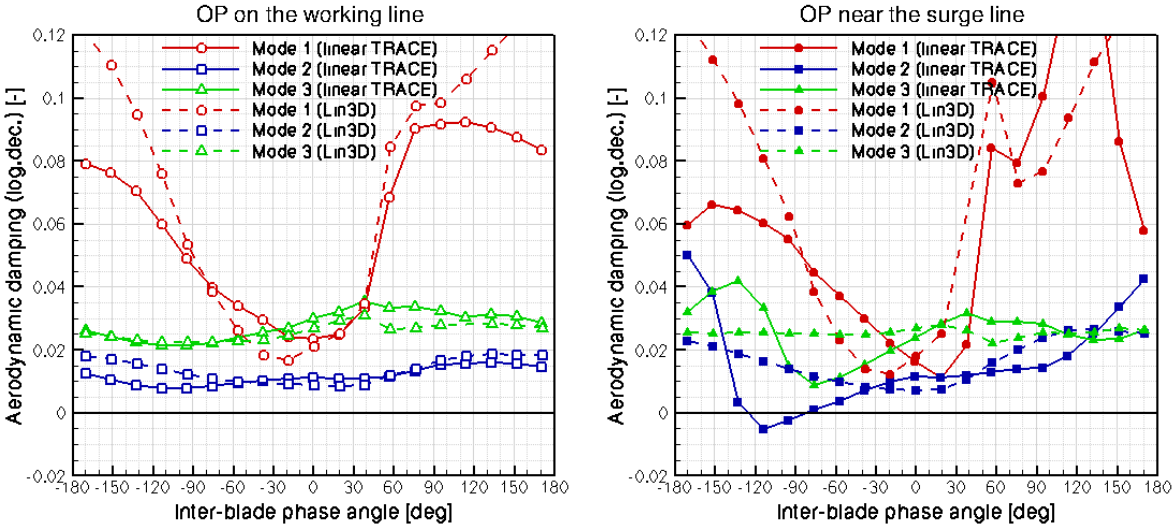

Figure 5: **Damping diagrams for the first three modes**

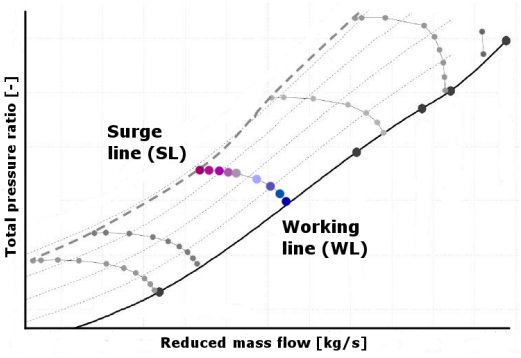

Figure 6: **Sketch of performance map**

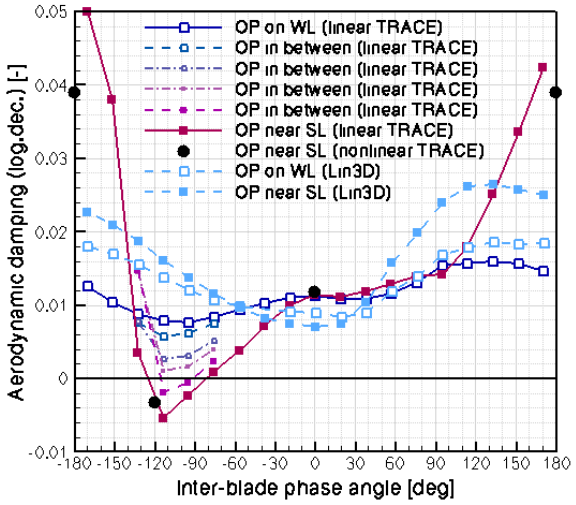

Figure 7: **Damping diagram for mode 2**

After mapping the surface displacements of the structural eigenmodes to the respective panels of the CFD mesh, the time-linearized flow solvers were applied to determine the unsteady pressure distribution on the blade surface for all IBPAs. It shall be pointed out that the DLR TRACE code as well as Lin3D from MTU Aero Engines were set up using the identical steady Navier-Stokes solution as basis for linearization.

Figure 5 compares the logarithmic decrement of the aerodynamic damping of the first three modes for two different operating points: one of them on the working line, the other one near the surge line. Apart from the deviations for the first mode at high inter-blade phase angles, a rather good agreement between linear TRACE and Lin3D can be observed for the WL (left diagram). However, the corresponding chart for the SL (on the right-hand side) shows a picture that is completely different: the two solvers do not coincide properly. Especially the second mode reveals a drastic drop in aerodynamic damping according to linear TRACE, leading to an aeroelastic instability.

Figure 7 illustrates that this phenomenon slowly arises from the working line while continuously throttling (cf. Figure 6), and thus is of physical origin. In addition, for the OP near the SL some nonlinear time domain simulations have been performed with a multi-passage setup (phase-lag boundary conditions led to a continuous increase in mass flow rate and thus change in operating conditions) in order to obtain reference solutions for specific IBPAs of the critical mode 2.

Local Comparison

Looking at the local contributions to aerodynamic work (and generalized aerodynamic force respectively) for mode 2 in Figure 8, one can identify the reason for the different damping values for the critical IBPA of $\sigma_n = -120°$. The work entry on pressure (PS) and suction side (SS) is nearly zero apart from the outer 15 percent of the blade – they represent roughly 80% of the global value indicating the importance of flow phenomena in this region.

According to linear TRACE the phase shift between unsteady pressure fluctuation and blade motion is such that the shock in front of the leading edge as well as the lambda shock on the profile excite the blade. In contrast, Lin3D predicts strong stabilizing effects in the region around the leading edge resulting from a different phase shift.

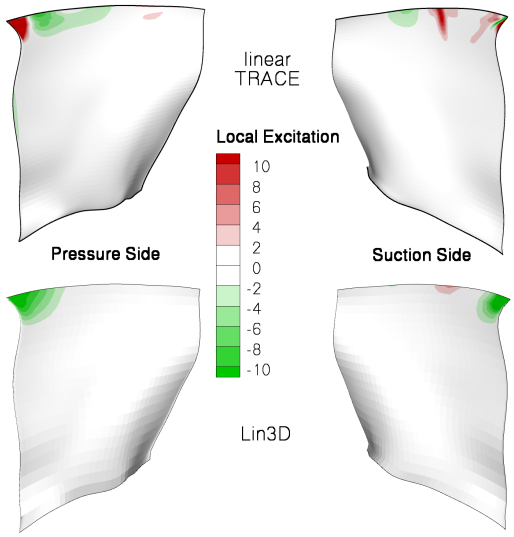

Figure 8: **Local excitation** ($\sigma_n = -120°$)

A detailed comparison of magnitude and phase angle (with respect to motion) of the unsteady pressure coefficient $\hat{C}_p = \frac{\hat{p}}{\hat{q}(p_{t1}-p_1)}$ can be found in Figure 9 for two different IBPAs of mode 2. For the purpose of clarity, the phase shift between motion and pressure response has been restricted to the interval $[-180°; +180°]$, so that a positive phase angle – in analogy to generalized aerodynamic forces – automatically indicates a destabilizing effect of the corresponding pressure amplitude. On the contrary, a negative angle in the lower plot results in a stabilizing contribution of the corresponding pressure value in the upper plot.

At midspan, the two solvers show similar results for the complex pressure amplitudes. Nevertheless a significant difference in magnitude has to be stated for the location of the lambda shock on the suction side. However, at 90% span the local unsteady flow solutions of linear TRACE and Lin3D are not comparable any more, neither for an inter-blade phase angle of $\sigma_n = -120°$ nor for $\sigma_n = 0°$, where at least a similar global damping value had been observed. Apart from the distinctive peaks of pressure magnitude in the linear TRACE results that are completely smeared in the Lin3D pressure

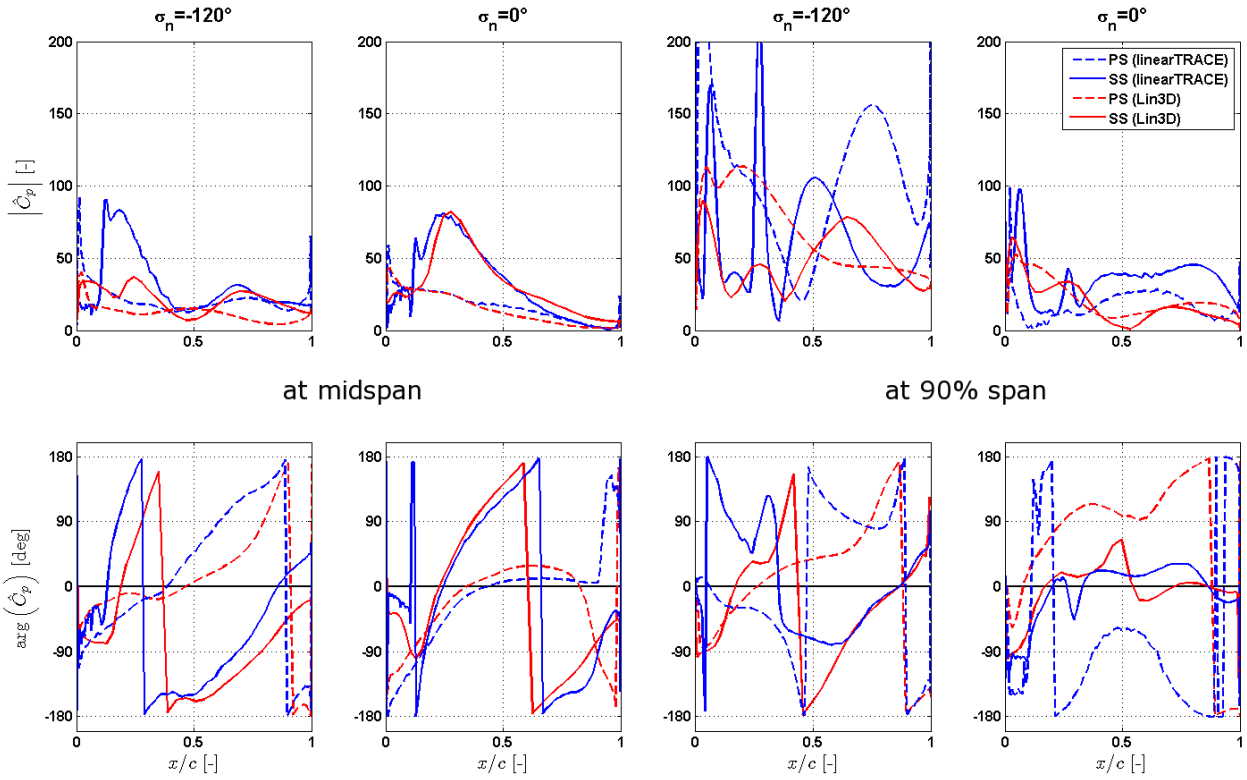

Figure 9: **Pressure coefficients for mode 2 at two different radial sections**

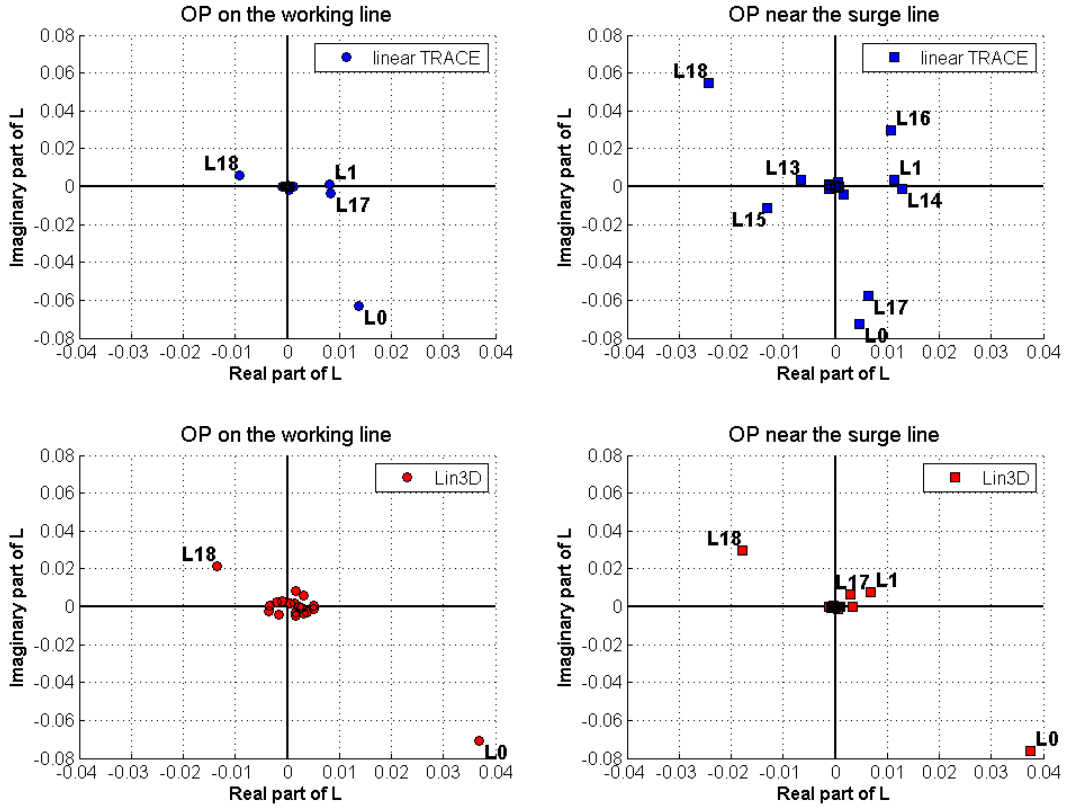

Figure 10: **Influence coefficients for mode 2 in the complex plane**

distribution, mainly the phase angles reveal drastic deviations over the chord length.
Since the tip region is responsible for roughly 80% of the complete energy transfer of mode 2, it is advisable to conduct further nonlinear flutter analyses in order to clarify whether there is a crucial influence of nonlinear unsteady phenomena such as tip gap vortices for instance.

Influence Coefficients

It is evident that the shock movement in the tip region is captured differently by the two solvers, which might have several reasons: the interpolation of the steady Navier-Stokes solution onto a coarser Euler grid in Lin3D, its lack of modeling the tip gap or even the neglect of viscous flux contributions $\frac{\partial \vec{F}_v}{\partial \vec{U}}$ in the time-linearized Euler calculations.
At least the first hypothesis can be proven true by applying the classical theory of influence coefficients. Figure 10 compares the complex influence coefficients for linear TRACE and Lin3D, once again for mode 2 at the two operating points on the working line and near the surge line. It is particularly striking that in the case of linear TRACE a higher number of L_i with significant amplitude is present. The vectors to these points are rotated in the complex plane with respect to the IBPA in order to determine the final stabilizing ($\Im < 0$) or destabilizing ($\Im > 0$) contribution. Only L_0 stays at its original position and thus the self-influence of a vibrating blade always has a stabilizing effect.
Recalling the steady flow solutions from Figure 3 and taking into account the ascending numbering of passages in downward direction, one can easily deduce the reason for the presence of the coefficients L_{18} to L_{13} for linear TRACE near the surge line. The respective blades 18 to 13 are located in direction of the suction side with respect to reference blade 0 and thus downstream of the stronger shock at this OP by whose harmonic motion they are affected. This phenomenon does not seem to be captured within Lin3D where much less influence coefficients are different from zero, probably because the coarse Euler grid is not able to resolve properly the small shock movement that is far away from the reference blade. Running linear TRACE in Euler mode on the fine Navier-Stokes mesh confirms this hypothesis: despite a generally bad convergence behaviour for the OP near the SL, the critical IBPA region for mode 2 comes up with several converged solutions with negative aerodynamic damping values; although the observed dip is shifted slightly towards the right.
Another interesting observation is not only the increasing number of influence coefficients for operating points near the surge line, but also their increased absolute value. Naturally this implies bigger changes of the global stability behaviour in regard to the IBPA – a fact that is confirmed by comparing the damping curves for operating points on the working line and near the surge line in Figure 5.

CONCLUSIONS

Time-linearized Euler and Navier-Stokes approaches have been compared for two operating points. Whereas a good agreement was found for the OP on the working line, significant differences had to be stated near the surge line. First of all, this concerns the tip region of the blade playing the decisive role with respect to aeroelastic stability of this configuration, a fact that was figured out by means of local work entries and pressure coefficients in radial sections for the second mode.
Moreover, the classical theory of influence coefficients demonstrated that in modern transonic compressors – especially for operating points near the surge line – a strong influence of a moving shock might be present in direction of the suction side, which is in contrast to the rapidly decreasing influence with increasing distance to the reference blade found in literature.
To obtain a nonlinear reference solution for the considered OP near the surge line selected inter-blade phase angles have been calculated with a multi-passage CFD setup whose results comply with the linear TRACE simulations at first glance. Further investigations based on phase-lag boundary conditions are planned: a detailed comparison IBPA by IBPA shall shed more light on the question whether potential tip gap vortices are crucial for the flutter stability of the blade at part speed.

ACKNOWLEDGEMENTS

The support of this work by the German Federal Ministry of Defence is gratefully acknowledged. Beyond that, the authors would like to thank all project partners from the participating departments.

REFERENCES

M.S. Campobasso and M.B. Giles. Stabilization of a Linearized Navier-Stokes Solver for Turbomachinery Aeroelasticity. In *Computational Fluid Dynamics 2002*. 2002.

F.O. Carta. Coupled Blade-Disk-Shroud Flutter Instabilities in Turbojet Engine. *Journal of Engineering for Power*, pages 419–426, July 1967.

F.O. Carta and A.O. St.Hilaire. Effect of Interblade Phase Angle and Incidence Angle on Cascade Pitching Stability. *ASME Journal of Engineering for Gas Turbines and Power*, 102:391–396, 1980.

W.S. Clark and K.C. Hall. A Time-Linearized Navier-Stokes Analysis of Stall Flutter. *Journal of Turbomachinery*, 122(3):467–476, 2000.

B. Hagenah. *Development and Application of a time-linearized 2D Euler Solver for Flutter Investigations in Turbomachines*. PhD thesis, RWTH Aachen, Germany, 2004.

K.C. Hall. *A Linearized Euler Analysis of Unsteady Flow in Turbomachinery*. PhD thesis, MIT Cambridge, USA, 1987.

Y. Hanamura, H. Tanaka, and Y. Yamaguchi. A Simplified Method to Measure Unsteady Forces Acting on the Vibrating Blades in Cascade. *Bulletin of JSME*, 23(180):880–887, 1980.

H. Hennings. *Experimental flutter investigations of a straight two-dimensional compressor cascade in incompressible flow*. PhD thesis, RWTH Aachen, Germany, 1997.

D.G. Holmes and C.B. Lorence. Three-Dimensional Linearized Navier-Stokes Calculations for Flutter and Forced Response. In T.H. Fransson, editor, *Unsteady Aerodynamics and Aeroelasticity of Turbomachines*, pages 211–224. Kluwer Academic Publishers, 1998.

G. Kahl. *Aeroelastic Effects of Mistuning and Coupling in Turbomachinery Bladings*. PhD thesis, EPF Lausanne, Switzerland, 2002.

R. Kemme. *Numerical Investigation of the Aeroelastic Stability Behaviour of a Highly Loaded Compressor Rotor*. PhD thesis, TU Hannover, Germany, 2004.

H.-P. Kersken, C. Frey, C. Voigt, and G. Ashcroft. Time-Linearized and Time-Accurate 3D RANS Methods for Aeroelastic Analysis in Turbomachinery. In *Proceedings of ASME Turbo Expo 2010 in Glasgow, UK*, 2010. Paper No. GT2010-22940.

F. Lane. System Mode Shapes in the Flutter of Compressor Blade Rows. *Journal of Aeronautical Sciences*, 23:54–66, January 1956.

M. May. Sensitivity Analysis with respect to Flutter-Free Design of Compressor Blades. In *Proceedings of ASME Turbo Expo 2010 in Glasgow, UK*, 2010. Paper No. GT2010-23557.

P. Petrie-Repar. Development of an Efficient and Robust Linearised Navier-Stokes Flow Solver. In J.P. Thomas K.C. Hall, R.E. Kielb, editor, *Unsteady Aerodynamics, Aeroacoustics and Aeroelasticity of Turbomachines*, volume VI, pages 437–448. Springer, 2006.

M.F. Platzer and F.O. Carta, editors. *Aeroelasticity in Axial-Flow Turbomachines*, volume Volume 1: Unsteady Turbomachinery Aerodynamics. Volume 2: Structural Dynamics and Aeroelasticity of *AGARDograph No. 298*. AGARD, 1987/88.

L. Sbardella and M. Imregun. Linearized Unsteady Viscous Turbomachinery Flows Using Hybrid Grids. *Journal of Turbomachinery*, 123(3):568–582, July 2001.

U. Siller and M. Aulich. Multidisciplinary 3D-Optimization of a Fan Stage Performance Map with Consideration of the Static and Dynamic Rotor Mechanics. In *Proceedings of ASME Turbo Expo 2010 in Glasgow, UK*, 2010. Paper No. GT2010-22792.

U. Siller, C. Voss, and E. Nicke. Automated Multidisciplinary Optimization of a Transonic Axial Compressor. In *Proceedings of AIAA Aerospace Sciences Meeting 2009 in Orlando, USA*, 2009. Paper No. AIAA2009-863.

P. Vasanthakumar, M. May, and J. Belz. Aeroelastic Stability Analysis of the AeroLight Rotor. Technical Report IB 232 - 2010 C 01, DLR German Aerospace Center – Institute of Aeroelasticity, Göttingen, Germany, 2010.

D. Vogt. *Experimental Investigation of Three-Dimensional Mechanisms in Low-Pressure Turbine Flutter*. PhD thesis, KTH Stockholm, Sweden, 2005.